REGULARIZED FINITE-ELEMENT GLOBAL RECONSTRUCTION FOR HIGH-FIDELITY OCT VIBROMETRY

PIETER LIVENS[1*], STÉPHANE AVRIL[2], SAM VAN DER JEUGHT[3], AND ADRIAN BRADU[4]

[1]Bio- & Medical physics lab (BIMEF), Groenenborgerlaan 171, Antwerp, Belgium
[2]Surface and Tissue engineering lab (STBio), Cr Faurie 158l, Saint-Étienne, France
[3]Industrial Vision lab (InViLab), Groenenborgerlaan 171, Antwerp, Belgium
[4]Applied Optics Group (AOG), School of Engineering, Mathematics and Physics, University of Kent, Canterbury, UK
**pieter.livens@uantwerpen.be*

Abstract

Optical Coherence Tomography (OCT) vibrometry provides sub-nanometer displacement sensitivity and has become a key technique for mapping complex vibration patterns, particularly in hearing research where frequency-dependent motion of middle-ear structures is central to diagnosing pathology. However, at high frequencies, OCT measurements often approach the noise floor, degrading the accuracy and interpretability of reconstructed displacement fields, which is especially critical for fast and reliable assessment.

We introduce a robust, regularized finite-element (FE) global reconstruction framework that utilizes higher-order shape functions and L-curve optimization to recover continuous, high-fidelity displacement fields. Through comprehensive simulation and experimental validation, we demonstrate that this method significantly outperforms traditional unregularized filters. Statistical validation via two-sample t-tests indicates that the regularized approach achieves significantly lower mean reconstruction errors compared to lower-order methods ($p < 0.01$). Most importantly, variance testing proves that regularized filtering always improves the variance ($p < 0.01$), consistently reducing noise-propagation while preserving the underlying accuracy of the reconstructed field. This workflow provides an objective, reproducible method for quantitative vibration analysis, bridging the gap between raw OCT data and high-fidelity mechanical modeling.

1. Introduction

Optical Coherence Tomography (OCT) provides high-resolution volumetric imaging based on backscattered light [1], achieving axial resolutions of 1-15 µm depending on system design and optical bandwidth. In ophthalmology, OCT is clinical standard for characterizing retinal layers [2,3]. Recent advances in image processing and super-resolution techniques have further improved its diagnostic capabilities even on standard hardware [3–7].

In addition to morphological imaging, the phase of the OCT signal can be analyzed to extract vibrational motion, enabling phase-sensitive OCT vibrometry with sub-nanometer displacement sensitivity [8,9]. Owing to this unique ability to combine morphological and vibrational information, OCT has generated significant interest in the field of hearing research [10,11]. For example, the inner ear, specifically the cochlea, has been investigated using OCT-vibrometry [12,13]. Furthermore, the workings of the middle ear, i.e., the eardrum and hearing ossicles, have also been investigated with great success [8,10,14].

However, one key challenge in middle ear studies is that eardrum displacements are extremely small and highly frequency dependent. For sound pressures near 1 Pa (94 dB SPL), displacements reach only a few hundred nanometers and rapidly decrease with frequency [15]. Consequently, measured vibration maps often exhibit a low signal-to-noise ratio, limiting accurate mode shape reconstruction and reducing diagnostic interpretability. While methods such as local Gaussian filtering or selection of the brightest voxels have been used to mitigate noise [8], [16], these local approaches inherently smooth data without reconstructing a continuous displacement field, making quantitative interpretation difficult.

An alternative to local data filtering methods are global least-squares approaches, which consider the entire dataset simultaneously. Among these, finite element (FE) approximation is particularly attractive because it provides a piecewise continuous reconstruction of the displacement field through element-based shape functions, inherently ensuring spatial smoothness. Moreover, this framework naturally integrates with standard FE software, facilitating subsequent mechanical modeling or material analysis [17–19]. FE-based global filtering has been shown to outperform local filters when processing full-field techniques such as Digital Image Correlation [19–22]. Recently, Livens and Ukshini (2025) compared local and global filtering strategies on Pressure-Sensitive Paint data, demonstrating that the FE approach can objectively balance noise suppression and spatial resolution via mesh and regularization control [23].

This paper addresses our limited knowledge of suitable filters for OCT data, and explores the application of regularized FE reconstruction to OCT displacement data. Low- and higher-order polynomial shape functions are evaluated in combination with Tikhonov regularization, enabling suppression of noise while maintaining spatial fidelity. The technique is validated through simulated and experimental case studies, including a vibrating rubber membrane and a rabbit eardrum, demonstrating its ability to reconstruct smooth, high-resolution displacement maps and to reveal frequency-dependent vibrational mode shapes under low signal-to-noise conditions. A set of MATLAB routines implementing the approach is freely available for research use: https://bitbucket.org/bimef/oct-filtering-using-global-fe/src/main/

2. Materials and methods

2.1 Finite element reconstruction of discrete data

Measured displacements d_i at locations $\boldsymbol{x}_i$ are inevitably affected by noise. Assuming zero mean additive Gaussian noise $\mathcal{N}_i$, with standard deviation σ, the relation between the ground truth displacement $u(\boldsymbol{x}_i)$ and the measured data can be expressed as:

$$d_i = u(\boldsymbol{x}_i) + \mathcal{N}_i(0, \sigma) \tag{1}$$

OCT vibrometry signals are affected by several noise sources, including phase jitter of the light source, shot noise, and mechanical vibrations of the measurement setup. Although these components are generally non-Gaussian, their combined effect can be considered additive and modeled as in Eq. (1). In the following, we denote this cumulative noise contribution as $\mathcal{N}_i$. Displacements d_i are a scalar quantity in this work, since OCT only measures displacements along the longitudinal direction. If the full 3D displacement field needs to be reconstructed, Eq. (1) can be repeated for each component of motion. In practice, the goal is to filter noise and reconstruct a smooth, continuous approximation of the true displacement field $u(\boldsymbol{x}_i)$. Local filters such as moving averages or Gaussian smoothing achieve this by averaging data within small neighborhoods. While simple to implement, these methods rely heavily on user-chosen parameters, and the resulting output is restricted to a discrete set of points, not a continuous field, which substantially limits interpretability and further analysis [20].

In contrast, global filtering methods use all measured data simultaneously to obtain a continuous reconstruction. Among these, FE reconstruction is particularly advantageous because it provides a piecewise continuous representation of the field via element shape functions and can be directly integrated with conventional FE software for subsequent analysis or modeling.

Given nodal displacements u_j and shape functions $N_j(\boldsymbol{x})$, the displacement field $u(\boldsymbol{x})$ can be approximated by:

$$u(\boldsymbol{x}) = \sum_{j=1}^{K} N_j(\boldsymbol{x}) u_j \tag{2}$$

Organizing all measurements in a vector $\boldsymbol{d}$, the nodal values in a vector $\boldsymbol{u}$ with corresponding noise $\boldsymbol{\mathcal{N}}$, and the selected shape functions into interpolation matrix M, Eq. (1) and (2) become:

$$\boldsymbol{d} = M\boldsymbol{u} + \boldsymbol{\mathcal{N}} \tag{3}$$

The least-squares solution seeks to minimize the residual between measured and reconstructed nodal displacements:

$$\min_{u} \| M\boldsymbol{u} - \boldsymbol{d} \| \tag{4}$$

yielding the following estimate $\widehat{\boldsymbol{u}}$ for the nodal displacements:

$$\widehat{\boldsymbol{u}} = (M^t M)^{-1} M^t \boldsymbol{d} \tag{5}$$

By inserting Eq. (3) into Eq. (5), the estimate becomes

$$\widehat{\boldsymbol{u}} = \boldsymbol{u} + (M^t M)^{-1} M^t \boldsymbol{\mathcal{N}} \tag{6}$$

Therefore, the reconstructed displacement field $\widehat{\boldsymbol{u}}$ is contaminated by a noise-propagation term that depends on both the noise vector $\boldsymbol{\mathcal{N}}$ and the conditioning of M.

To stabilize the inversion, Tikhonov regularization introduces an additional penalty term to Eq. (5) that enforces smoothness in the displacement field [24]

$$\widehat{\boldsymbol{u}} = (M^t M + \lambda L^t L)^{-1} M^t \boldsymbol{d} \tag{7}$$

The regularization matrix L and regularization strength λ control the balance between fidelity to measured data $\boldsymbol{d}$ and smoothness of the reconstruction $\widehat{\boldsymbol{u}}$. Using the second order derivative operator as regularization matrix has been shown to improve data reconstruction in Digital Image Correlation [25,26], spline interpolation [27], and when processing pressure-sensitive paint data [23]. In this paper, we will follow a similar approach and regularize the solution using the following expression

$$\widehat{\boldsymbol{u}}_\lambda = \left(M^t M + \lambda \left(\frac{\partial^2 M}{\partial^2 x^2} \right)^{\boldsymbol{t}} \frac{\partial^2 M}{\partial^2 x^2} \right)^{-1} M^t \boldsymbol{d} \tag{8}$$

Filtering performance, therefore, depends on three main parameters:

1. **Element size**, which defines the spatial averaging scale and determines how much data is included within each element.
2. **Shape function order**, which controls the complexity of the displacement reconstruction within each element. Higher-order functions capture finer spatial variations but are more sensitive to noise.
3. **Regularization strength**, which governs the degree of smoothing applied to the reconstructed field.

All three parameters can be set objectively using L-curve analysis [23,25], which plots the residual norm $\|M\widehat{\boldsymbol{u}}_\lambda - \boldsymbol{d}\|$ against the smoothness term $\|L\widehat{\boldsymbol{u}}_\lambda\|$. Such curves often represent the letter L, and the point of maximum curvature represents the best trade-off between fidelity to the data and suppression of noise. Examples of L-curves are given in the Appendix, and more details about their interpretation follow in the Results section.

2.2 Simulation experiments

To validate the finite element reconstruction approach, we first created two simulation datasets. Both datasets were created using finite element simulation in COMSOL Multiphysics (V6.2).

The first model is illustrated in Fig. 1A: a circular membrane with a radius of 5 mm. A thickness of 80 µm, stiffness of 100 MPa, and Poisson's ratio of 0.3 were defined, so the simulated output resembles that of the nitril rubber used in the experiments. A pressure wave of 82 dB SPL is applied to the membrane's surface. The outer edge of the membrane was fully fixed, i.e., no rotations or displacements were allowed. The model was solved for frequencies of 1000, 2400, and 3600 Hz. The resulting complex-valued displacement data was exported to MATLAB (R2024a).

The second model is that of a human middle ear, which has been described in other works [28,29]. The eardrum, shown in red in Fig. 1B, has an elliptical shape with major and minor axes of 5 and 4.4 mm, respectively. The eardrum's stiffness was set to 30 MPa, Poisson's ratio to 0.3, and the thickness to 80 µm. A pressure load of 82 dB SPL was defined at the lateral surface (ear canal side), and the model was solved for frequencies of 2000, 2500, and 4000 Hz. The resulting complex-valued displacement data was exported to MATLAB.

For both datasets, we used MATLAB's *scatteredInterpolant* method with linear interpolation to resample the finite element data to voxel locations representing an OCT volume. A typical B-scan in our experimental setup had 200 axial by 130 lateral pixels, respectively. The *experimental* volume was constructed by collecting 50 B-scans at different Y coordinates across the volume. Therefore, the finite element data was interpolated to resemble the experimental data. The X, Y, and Z coordinates were resampled to a grid of size 130, 50, and 200, respectively. The corresponding X, Y, and Z spatial resolution for both datasets was 89, 224, and 5 µm, respectively.

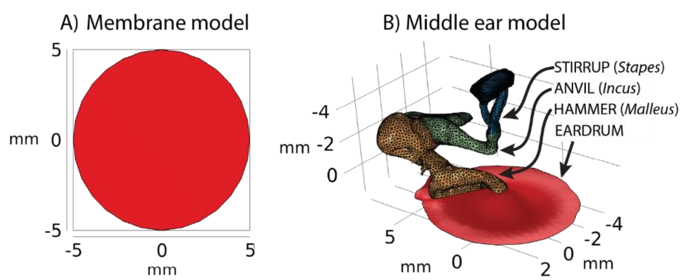

Fig. 1. Overview of the two simulated dataset: a circular rubber membrane (A), and a human middle ear (B).

Sensitivity analysis of the experimental OCT data demonstrated that the setup can resolve displacements as small as 5 nm at frequencies below 1 kHz. Although the noise floor decreases at higher frequencies, the analysis focused on the worst-case scenario. Therefore, 5 nm Gaussian noise was added to the simulated OCT volumes to mimic the noise present in an experimental dataset. The noisy simulated experimental data is shown in Fig. 2. The top row shows data of the membrane, and the bottom row shows the eardrum data. When comparing data from left to right in Fig. 2, we see that when the input sound frequency increases, the displacement maps become more complicated. Additionally, the displacement amplitude quickly decreases with increasing frequency, leading to increasingly noisy data.

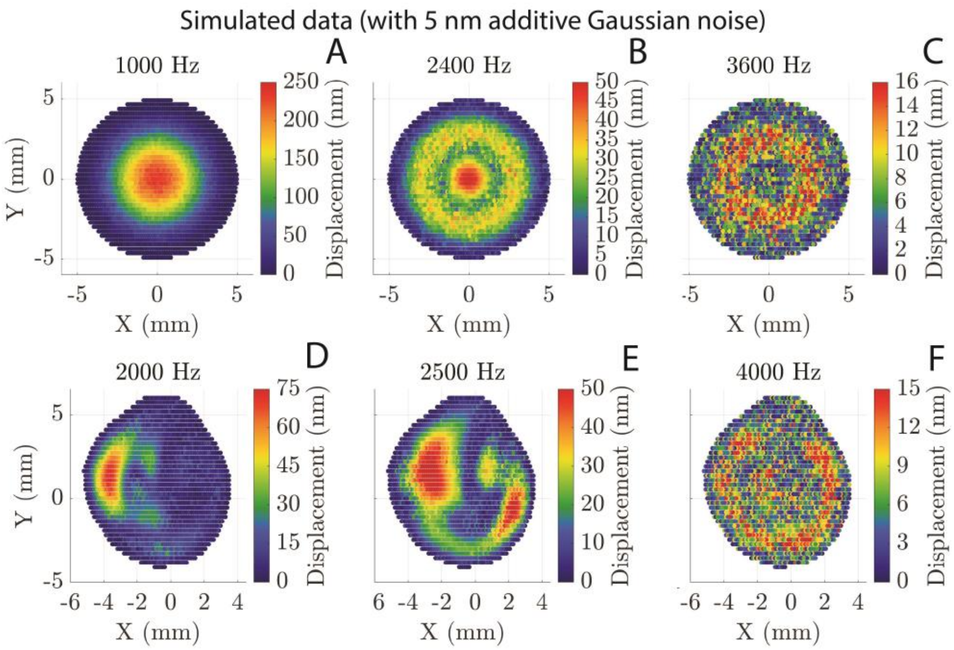

Fig. 2. Simulated data for the circular membrane (top) and eardrum (bottom). Increasing the frequency of the input pressure leads to more complicated modal behavior (left to right). Due to the rapid decrease in displacement amplitude with frequency, the higher frequency data is much noisier.

2.2 Optical coherence tomography measurements

Sample preparation

To complement the simulations, two objects were examined using OCT vibrometry: a rubber membrane and a rabbit eardrum.

A patch of nitril rubber (VWR, serial nr. 112-2372) was stretched across a metal cylinder with a hollow inner bore of 5 mm radius, see Fig. 3A. The outer radius of the holder was 15 mm. The membrane was fixed using a metal washer bolted to the cylinder top, ensuring uniform tension without visible wrinkling. Two openings were made along the cylinder's length: one opening to connect an earbud (Sennheiser, CX 300 II) for sound stimulation, and a second opening allowed the probe microphone (Brüel & Kjær, type 4182) to record the acoustic pressure. The cylinder was then fixed on a translation stage using double-sided tape and placed underneath the OCT imaging head, with the membrane oriented perpendicular to the optical axis.

To collect eardrum data, we obtained a rabbit head from a local breeder (Peeters – Verbaeten, Ranst, Belgium), immediately frozen after death. The head was thawed at room temperature for one hour, after which the ear canal was removed to allow visual access to the eardrum. The preparatory steps to remove the ear canal, allowing visual access to the eardrum, have been described elsewhere [30–32]. The middle ear chain was left intact, and only bony parts of the ear canal wall limiting optical access were removed, (illustration in Fig. 3B). To stimulate the eardrum, a hole was made in the middle ear cavity. Then, a 3D printed microphone and speaker connector was positioned over the hole and sealed using two-component silicone paste (Dreve Otoplastik, Otoform Ak X), ensuring an airtight connection. The sample was then fixed on a holding stage using mechanical clamps to minimize motion and placed beneath the OCT imaging head, as shown in Fig. 3C.

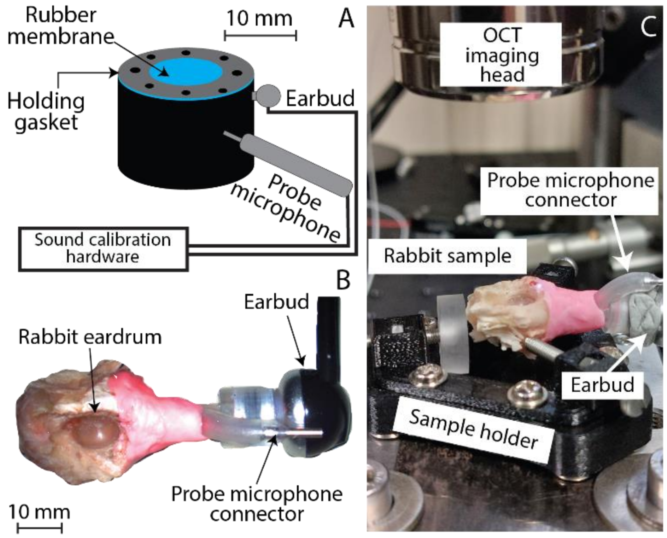

Fig. 3. Schematic of the measured membrane (A) and a picture of the prepared eardrum (B). An earbud and probe microphone are connected to calibrate the sound pressure level. The samples are positioned in the OCT-vibrometry setup using a custom sample holder.

Experimental OCT setup & data processing

To measure the displacement maps resulting from the acoustic pressure, a custom spectral domain OCT-vibrometry setup was developed. The instrument uses a superluminescent diode as an optical source, with a central wavelength of 840 nm and a 50 nm spectral bandwidth (Superlum Broadlighter, model S840). The axial resolution, determined using this source, experimentally measured, was 5 µm (in biological tissue). In the sample arm, two orthogonal galvanometer mirrors (Thorlabs, model GVS002) were used to scan the optical beam over the sample. The beam was focused onto the sample by a 54 mm focal length scan lens (Thorlabs, LSM04-BB). Light back-scattered by the sample was then recombined with the light from the reference arm and detected by an in-house devised spectrometer. The spectrometer includes a transmission diffraction grating from Wasatch Photonics with 1,200 lpm, which diffracts the optical beam over the pixels of a fast line camera (Teledyne e2v, model Octoplus USB). Positioning of the galvanometers and triggering of the line cameras is done via a multifunction I/O device (National Instruments, model PCIe-6321) and custom LabVIEW software. The acquisition rate of the camera was 100 kHz, i.e., every 10 µs, an OCT intensity profile is collected. Intensity OCT images were produced using the Master-Slave approach [35] and displayed in real-time.

OCT-vibrometry uses fluctuations in the phase of interferometric signals to measure vibrations and movements of scatterers within a medium. To employ this method, the setup was modified to allow for measurements of both the magnitude and phase of the OCT interferometric signal in synchronism with an acoustic stimulus. When an acoustic stimulus, such as a sinusoidal sound wave, is applied, it causes oscillations of the scatterers, leading to a change in the OCT signal's phase. By capturing consecutive OCT reflectivity profiles (A-scans), at central wavelength λ_c, the phase difference $\Delta\Phi(\mathrm{t})$ can be calculated. Mathematically, the displacement of the scatterer $\Delta\mathrm{z}(\mathrm{t})$, can be expressed as [33–35]

$$\Delta\mathrm{z}(\mathrm{t}) = \frac{\lambda_c}{4\pi}\Delta\Phi(\mathrm{t}) \quad (9)$$

A laptop connected to a terminal block (National instruments, USB-6251) was first used to calibrate the earbud speaker voltage using the probe microphone to reach 82 dB SPL for each desired frequency of sound. Then, a 5 ms sound signal and a corresponding phase-locked trigger signal were created. The LabVIEW OCT software was modified so that the OCT instrument starts collecting data locked to the sound phase, and then collects 500 subsequent channeled spectra at each (x,y) position of the optical beam on the sample. As a result, because the camera operates at 100 Hz, a 1D vibrometry scan (in the z-direction) is obtained with data collected within 5 ms. The 5 ms duration was chosen because it allows us to quickly change the desired frequency without significant modifications to the hardware or software. The only stipulation is that the selected sound frequency must be a multiple of 200 Hz (5 ms period), so it is always contained wholly within the 5 ms interval.

Data necessary to construct a 2D vibrometry cross-sectional image (in the xz-plane) was acquired in 130x5 = 650 ms (X-galvo scanner driven at ~1.54 Hz). Finally, data were acquired to build a 3D vibrometry image at 50x0.65 = 32.5 s (Y-galvo scanner driven at ~0.03 Hz). We limited the number of 2D vibrometry images within the 3D volume to 50 because this provides a good balance between measurement duration, data size, and spatial resolution.

The real-time operation of the instrument was facilitated by the Master-Slave approach, which computes intensity and phase values only within the axial imaging range of interest, thereby limiting the number of axial points to a much smaller value than when using FFT-based techniques [36–38]. Thus, we only used 200 axial points in our images. As a result, the final volumetric vibrometry image was of 130x50x200 pixels. The field of view was the same for both the membrane and the eardrum data collection, and the corresponding spatial resolutions for the X, Y, and Z coordinates were 89, 224, and 5 µm, respectively.

Although the data acquisition time was only 32.5 s and the processing time to calculate the intensity and phase was very short, altogether, the time elapsed between the start of the data acquisition and the moment when the data are available on the hard drive to be processed in MATLAB was about 5 minutes due to the need to write large files to disk.

Withing dedicated segmentation software (Dragonfly 3D, V2024.1), Otsu thresholding and manual outlier removal, was used to create a binary mask separating the measured object from the background. This mask was then used in MATLAB to compute the FFT on the OCT phase data of the measured sample. The resulting displacement maps are shown in Fig. 4 for the membrane (top row) and for the eardrum (bottom row). For low frequencies, the displacement amplitudes are high and these data have good signal-to-noise ratio. However, at high frequencies the displacement amplitude becomes comparable to the noise floor, resulting in a reduced signal-to-noise ratio. Figure 4F is especially noisy, highlighting the need for dedicated filtering.

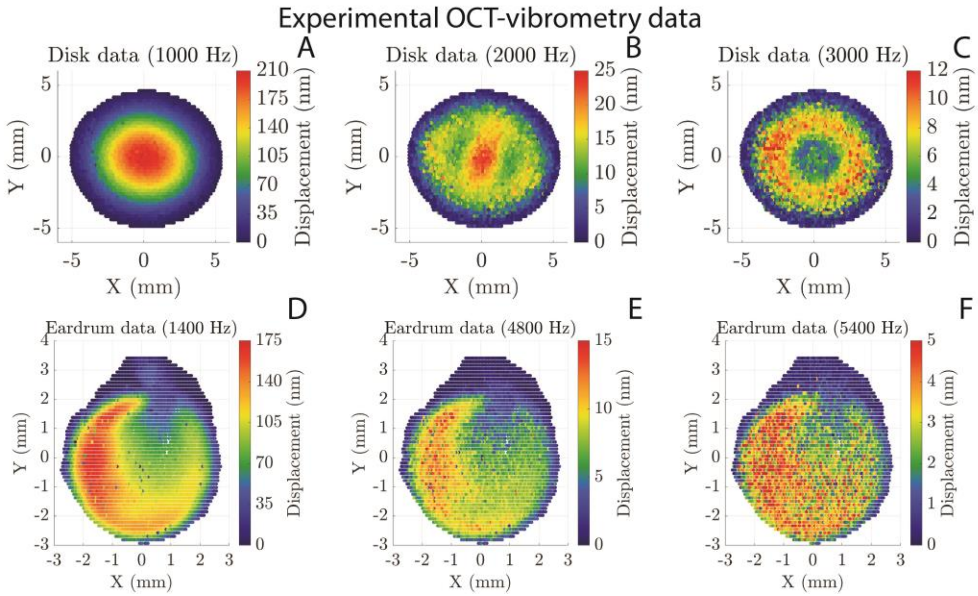

Fig. 4. Experimental data collected using our OCT-vibrometry setup of the rubber membrane (top) and the rabbit eardrum (bottom). Increasing the frequency of the input pressure leads to more complicated modal behavior (left to right). Due to the rapid decrease in displacement amplitude with frequency, the higher frequency data is much noisier.

3. Results

To reconstruct and filter data using Eq. (8), a suitable finite element mesh needs to be selected. Since our samples are very thin, we opted to use a mesh of surface elements to reconstruct the data. Through-thickness variations can then be visualized by scaling the displacement along the element's normal [39], but we will only present data on the middle surface of the objects. When the surface is meshed using triangular elements, abbreviated T3 onwards, there are three nodes per element, and three linear shape functions. A quadratic element can be defined by adding nodes at the midpoints of the triangle's edges, creating a quadratic T6 element. Similarly, a quadrilateral element has four nodes and bilinear shape functions, abbreviated Q4 onwards. By adding nodes to the midpoints of the Q4 edges, and one additional point at the element's center, the quadratic Q9 element can be defined. Going forward, we will systematically compare how T3 and Q4 elements compare with T6 or Q9, and what the effect of regularization is. When no regularization is used, we will denote the filtered result with $\lambda = 0$, while the regularized filtered data will be denoted with $\lambda = \lambda^*$, which is the value found by the L-curve. Both simulated and experimental datasets were processed using low-order, high-order, and regularized high-order filters to assess reconstruction quality.

Reconstructing simulation data

For the membrane data, a mesh was constructed using Q9 elements. Following Livens and Ukshini, we started with a mesh of 2 mm, but observed a downward sloping straight-lined curve and not an L-shaped profile. [23]. Decreasing the mesh size to 1 mm did produce the L-shaped profile, which is used in subsequent analysis. The L-curve at 3600 Hz is given as an example in the Appendix, Fig. A1.

Since the eardrum has a complicated cone-like shape, quadrilateral elements lead to very poor meshes with distorted elements. Therefore, a T6 element to mesh the eardrum data was employed. Using the L-curves, we found that a mesh with a size of 0.8 mm was the best suited, see Fig. A1.

The results of finite element filtering are shown in Fig. 5 for the membrane data (top) and the eardrum data (bottom). Compared with the noisy data (second column), all filter approaches work reasonably well. The (bi)linear elements (Q4 and T3) result in a smooth reconstruction but lose spatial detail. The quadratic elements (Q9 and T6) without regularization ($\lambda = 0$) provide a reconstruction with higher spatial resolution, but the results are noisier. When using the regularized reconstruction, smooth results with high spatial resolution are obtained.

To objectively quantify each filtering approach, the reconstruction error was computed as the absolute distance between the reconstructed and ground truth data. In Fig. 6, the reconstruction errors are shown as boxplots, grouped per frequency. Overall, Q4 or T3 elements (blue boxes) exhibit higher reconstruction errors and larger spread compared to Q9 or T6 elements (orange and yellow boxes), indicating both greater error and increased variability.

A two-sample t-test confirms that Q4 and T3 yield significantly higher mean reconstruction errors than Q9 ($\lambda = \lambda^*$) or T6 ($\lambda = \lambda^*$) ($p < 0.01$), while variance testing shows that differences in noisiness also contribute to the observed spread. For the rubber membrane data (Fig. 6A), at 1000 Hz, Q4 differs significantly from Q9 ($\lambda = \lambda^*$) in both mean and variance ($p < 0.01$). In contrast, Q9 ($\lambda = 0$) and Q9 ($\lambda = \lambda^*$) show no significant difference in mean ($p = 0.0539$) but a significant difference in variance ($p < 0.01$), indicating that regularization mainly reduces noise without affecting the average error. At 2400 Hz and 3600 Hz, both the mean and variance differ significantly across comparisons ($p < 0.05$), showing that regularization impacts both error magnitude and variability at higher frequencies.

For the eardrum data (Fig. 6B), T3 shows significantly higher mean error and variance than T6 ($\lambda = \lambda^*$) at all frequencies ($p < 0.01$). Comparing T6 ($\lambda = 0$) and T6 ($\lambda = \lambda^*$), no significant differences in mean or variance are observed at 2000 Hz and 2500 Hz ($p > 0.05$), indicating similar performance. At 4000 Hz, the mean remains unchanged ($p = 0.4556$), but variance differs significantly ($p < 0.01$), showing that regularization reduces noise without affecting the average error. In all cases, reconstruction errors remain well below the noise amplitude of 5 nm.

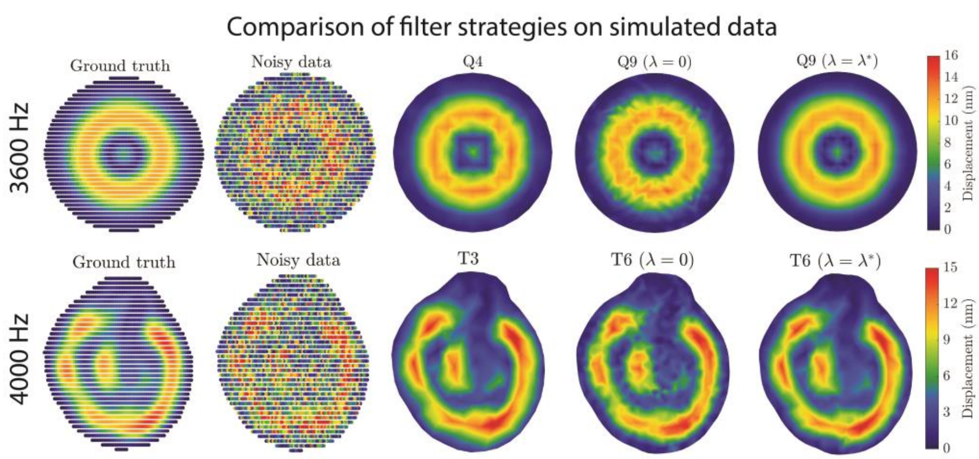

Fig. 5. Comparison of filtering approaches applied to the simulated data of the rubber membrane (top row) and the human eardrum (bottom row). The columns show the noisy input data (second column), reconstructions using Q4 and T3 elements (third column), higher-order elements without regularization (Q9 and T6, $\lambda = 0$; fourth column), and higher-order elements with regularization ($\lambda = \lambda^*$; last column).

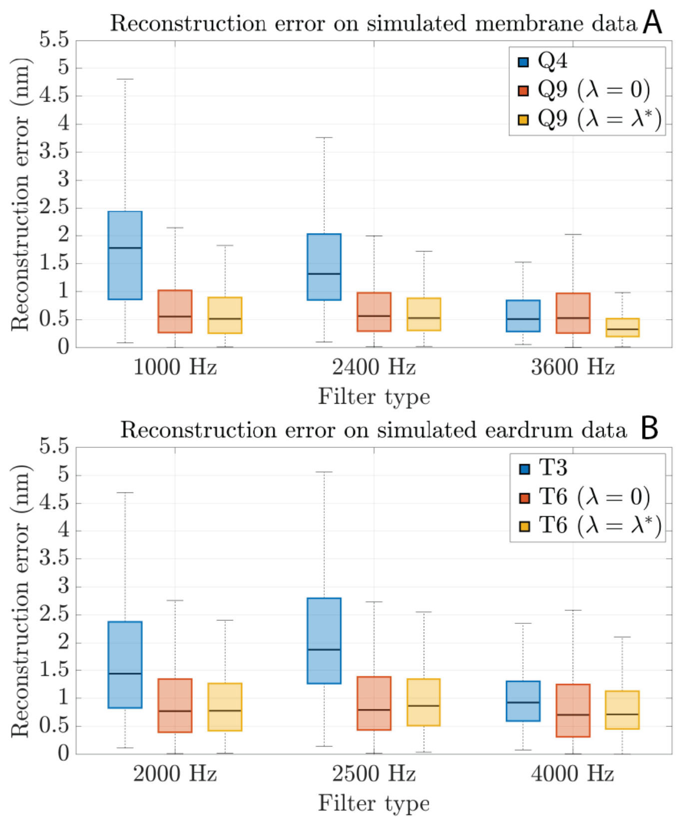

Fig. 6. Comparison of the reconstruction error on the membrane data (A), and the eardrum data (B). Filtering using Q4 or T3 elements (blue boxes) results in higher reconstruction errors compared to the Q9 or T6 element (orange and yellow boxes). At 3600 Hz, the unregularized Q9 ($\lambda = 0$) result (orange box) has higher whiskers than the Q4 (blue box), showing that higher order elements cause noisier reconstructions (A). The regularized approach Q9 ($\lambda = \lambda^*$, yellow box) leads to the best reconstruction. For the eardrum, the same results are observed (B).

Reconstructing OCT vibrometry data

Next, we applied the filtering procedure to the experimental OCT data shown in Fig. 4. For the rubber membrane data, a mesh size of 1 mm yields an L-curve with a distinct transition between the data fidelity and regularization regimes, consistent with the behavior observed in the simulated data (Fig. A2A). Coarser meshes produced more gradually descending curves without a clearly distinguishable transition. This indicates that the 1 mm mesh provides an appropriate balance between reconstruction accuracy and regularization at this spatial resolution.

Since rabbit eardrums are smaller than human eardrums, a finer discretization is expected. This is confirmed by the L-curve analysis, where coarser meshes again result in a less distinct transition between the two competing terms (Fig. A2B). Based on this analysis, we select a mesh size of 0.5 mm for further processing, noting that nearby values (e.g. 0.7 mm) yield comparable L-curve behavior and do not significantly affect the reconstructed results.

The filtered results are shown in Fig. 7 for the rubber membrane at 3000 Hz (top row), and for the rabbit eardrum at 5400 Hz (bottom row). For the rubber membrane data, the Q4 interpolation (top row, second column) produces a reconstruction with lower spatial variability than the higher-order Q9 approaches, but also attenuates fine spatial features. In contrast, the unregularized Q9 reconstruction ($\lambda = 0$; top row, third column) exhibits substantially larger variability than the regularized Q9 ($\lambda = \lambda^*$) result. Statistical analysis confirms that both the mean and variance differ significantly between these two reconstructions ($p < 0.01$), with the standard deviation decreasing from 3.89×10^{-9} m in the unregularized case to 7.89×10^{-10} m after regularization. The regularized Q9 reconstruction maintains the fine spatial structure while substantially reducing the spread of the displacement distribution. Similar trends are observed for the rabbit eardrum data (bottom row), where the standard deviation decreases from 1.36×10^{-9} m to 3.79×10^{-10} m with regularization ($p < 0.01$). Overall, these quantitative results demonstrate that regularization reduces variability in the reconstructed displacement fields while preserving the overall spatial reconstruction characteristics.

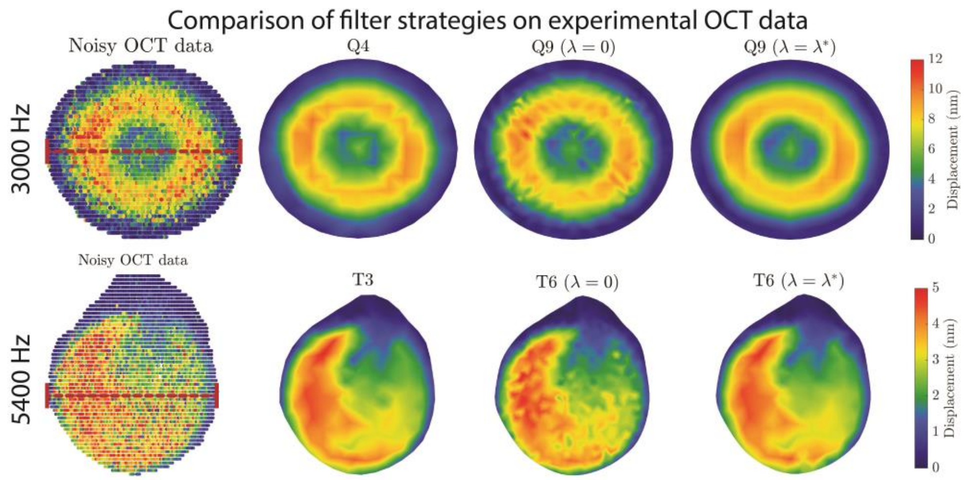

Fig. 7. Comparison of filters on the experimental data of the membrane (top) and the eardrum (bottom). For the rubber membrane (top row), the Q4 filter yields a smooth reconstruction but at reduced spatial resolution. The data filtered via the Q9 mesh without regularization ($\lambda = 0$) is quite noisy, while the regularized result is smoother and has higher spatial resolution. For the eardrum data, we see similarly that the regularized T6 filter ($\lambda = \lambda^*$) leads to the best reconstruction. The dashed lines in the first column indicate data locations used in the line plot of Fig. 8.

Since no ground truth data exists for the experimental data, we sought to compare the effects of different filters using a relative comparison. Data were selected along a horizontal line with coordinates Y=0, as indicated in Fig. 7, for both experiments. These data are presented in Fig. 8. For the membrane data at 3000 Hz, Fig. 8A, the experimental data (grey spheres) contain three distinct local maxima. The Q4 filter (orange line) underestimates these maxima, while the Q9 ($\lambda = 0$) filter (yellow line) follows the overall shape more closely but shows increased local oscillations. The Q9 ($\lambda = \lambda^*$) filter (purple line) provides a smoother reconstruction while maintaining the main features. Although visual differences between the Q9 filters are subtle, the statistical analysis described previously indicated significant differences in both mean and variance.

For the rabbit eardrum at 5400 Hz (Fig. 8B), the experimental data (grey spheres) are more sparsely distributed compared to the rubber membrane due to the thinner structure. The T3 filter (orange line) and T6 ($\lambda = \lambda^*$) filter (purple line) yield smooth and comparable reconstructions. In contrast, the T6 ($\lambda = 0$) filter (yellow line) exhibits pronounced oscillations along the profile, indicating increased sensitivity to noise with limited data. This observation is supported by the statistical results reported for Fig. 7 showing significant differences in both mean and variance, with the unregularized case exhibiting substantially higher variability.

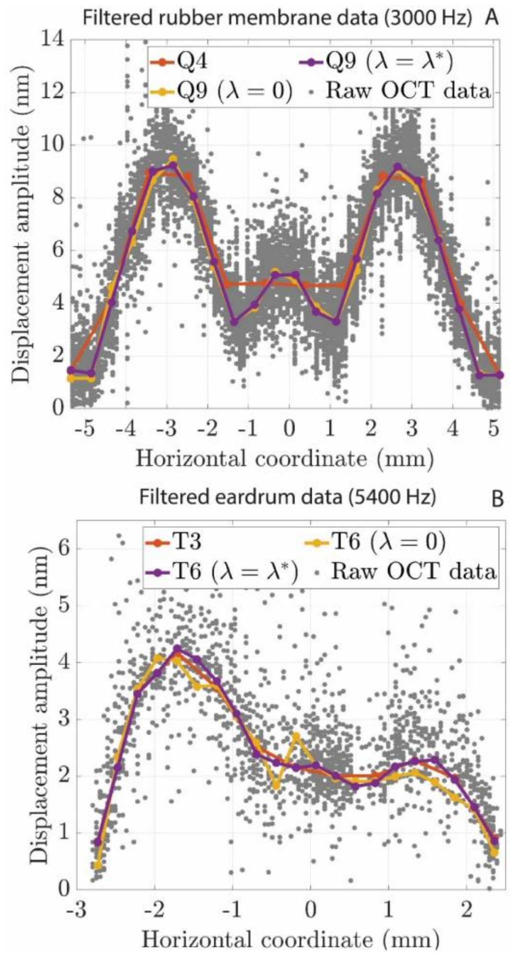

Fig. 8. Visualization of the OCT data (grey spheres) and the filtered output along a horizontal line Y=0 across the surfaces. For the rubber membrane (A), the experimental data at 3000 Hz shows three distinct maxima. The Q4 filter (orange) does not adequately capture this information. The regularized Q9 ($\lambda = \lambda^*$) filter (purple) approximate the data the best. For the thin rabbit eardrum, there are less datapoints (grey spheres) available (B). The T3 (orange) and T6 ($\lambda = \lambda^*$) filters show the smoothest approximation of the data. The T6 ($\lambda = 0$) filter is heavily influenced by noise, partially due to the limited amount of data.

4. Discussion

This study investigated the application of regularized finite element reconstruction of OCT displacement data. Simulated data demonstrated that regularized filtering with high-order polynomial shapes yielded the most accurate displacement field reconstructions. At low displacement amplitudes, the poor signal-to-noise ratio required filter regularization to prevent excessive noise in the results. Experimental OCT data were also analysed, and both filtered displacement maps and inspections across a line on the surface indicated that the regularized global filter perform better than unregularized low ordered shape functions. This study examined the efficacy of several global finite element-based filters, excluding comparisons with other commonly used filters such as local Gaussian averaging due to the following considerations:

1. The present study focuses on a finite element–based reconstruction framework in which smoothness is controlled through element order and regularization (via the L-curve), rather than through an explicitly defined spatial kernel size. This makes the parameterization fundamentally different: Gaussian filtering requires a chosen window size that directly sets the spatial cutoff, whereas in the proposed method smoothness emerges from the basis functions and regularization strength within the reconstruction problem itself. For this reason, a direct one-to-one comparison of parameter settings is not straightforward, even though both approaches influence spatial gradients in a related way.
2. Comparing local and global filters has been done before on other types of datasets, and the general consensus is that global filtering leads to more accurate result [17,20,21,23]. However, much less literature exists on *regularized* global filters. To the best of the authors knowledge, no paper has explored the use of global filtering on OCT vibrometry data, especially not including a regularized approach.
3. The result of global finite element filtering is a finite element mesh with nodal displacement values. These data can be readily compared to finite element models, enabling material characterization and accurate test-design-built cycles. Such an approach can be a powerful tool in developing robust data inspection pipelines.

We acknowledge that investigating a wider range of filter strategies would be valuable, but this is beyond the scope of the present paper.

One current limitation of global approaches is the requirement to generate suitable finite element meshes to use as filters. Evidently, mesh-quality directly influences the accuracy of the resulting displacement fields [40] From the OCT segmentations, the meshes for the rubber membrane could be easily constructed. The rabbit eardrum, however, has regions of only 30 μm thick [31]. Therefore, the initial mesh was quite noisy, and some additional steps such as Gaussian smoothing of the spatial coordinates and remeshing were required to generate a suitable mesh for interpolation. In future work, it could be convenient to generate a mesh-template which is then mapped onto the specific OCT dataset. Moreover, segmenting OCT data has been semi-automated using machine learning approaches [41,42]. Mesh generation could also be improved in this manner, provided a large enough training dataset can be acquired [43].

Although visualization of the L-curves is a convenient way to select the optimal mesh size and corresponding filter strength, there is still some level of subjectivity. The simulated data showed a clear L-curve, see Fig. A1. The experimental membrane data showed a clear L-curve, see Fig. A2 (A). However, the eardrum data's L-curve was not sharply defined for any of the mesh sizes studied, see Fig. A2 (B), presumably due to the low spatial density of the thin eardrum's OCT data. To check the robustness of our results, we varied the regularization strength λ around their selected values and found no significant changes to our results. Therefore, even when the L-curve is not well-defined, a sub-optimal choice still leads to significant noise reduction and accurate reconstructions.

One future improvement to make the λ selection more objective might be to compute the curvature of the L-curve, since the λ value resulting in maximal curvature corresponds to the location of the bend [25,44]. An alternative is to reformulate Eq. (8) as a constrained optimization problem [24], which can also enable automatic λ selection. Since this paper explored if (regularized) finite element approximation was a viable filter strategy for OCT data, we explicitly constructed the L-curve to inspect the optimal element size and smoothing strength λ, as was done in [23]. Therefore, an interesting future research goal might be to automate both the element size and λ selection at once.

While individual noise components such as shot noise and phase jitter are inherently non-Gaussian at the OCT voxel level, the application of Tikhonov regularization remains statistically sound due to the signal processing workflow. Because the displacement amplitude is derived via the Fourier transform of the temporal samples, the resulting aggregate noise term approximates a Gaussian distribution according to the Central Limit Theorem. Furthermore, the second-order derivative regularization serves as an effective spatial low-pass filter, penalizing high-frequency "spikes" and uncorrelated fluctuations. This ensures the reconstructed field maintains the spatial continuity expected of biological tissues, regardless of the underlying noise distribution, and explains the significant reduction in variance observed in our results ($p < 0.01$).

The proposed method and OCT setup show limitations in the high-frequency regime, where both simulations and experiments indicate that regularization becomes essential for suppressing noise. While regularization improves data reconstruction, the approach remains sensitive to acquisition constraints at high frequencies and low vibration amplitudes. This limitation is particularly evident in thinner structures such as the eardrum, where reduced signal levels due to optical transparency degrade data quality. These findings suggest that performance may decline in applications involving small-amplitude, high-frequency motion. Future improvements should therefore focus on increasing temporal sampling rates (e.g., below 5 μs) and employing OCT systems with shorter central wavelengths to enhance both temporal and spatial resolution, combined with regularized data filtering to maximize data fidelity.

The proposed framework is not limited to middle ear applications and may be extended to other biomedical contexts involving small-amplitude vibrations. Potential applications include ophthalmology (e.g., corneal or retinal motion) and cardiovascular biomechanics (e.g., vessel wall dynamics). In such cases, a separate L-curve analysis will need to be performed to determine the optimal mesh size and regularization strength. Nonetheless, the underlying approach to spatially regularized reconstruction remains directly applicable.

5. Conclusion

This work demonstrates the first successful application of regularized finite-element (FE) global reconstruction to OCT vibrometry. The approach effectively suppresses measurement noise and recovers continuous displacement fields with high spatial fidelity. Through simulations and experimental validation on a vibrating membrane and a rabbit eardrum, we show that regularized higher-order FE filters outperform low-order and unregularized methods in terms of smoothness, spatial resolution, and quantitative accuracy.

A central strength of the method is its objective parameter selection: mesh size, shape-function order, and regularization strength can all be determined via L-curve analysis, removing subjective tuning and enabling reproducible post-processing. While widely applicable to full-field displacement measurements, the technique is particularly well suited for hearing research, where resolving nanometer-scale, frequency-dependent eardrum motion is essential. By enabling robust and quantitative reconstruction, this method has the potential to advance diagnostic assessment of middle-ear disorders and improve the validation of biomechanical ear models. Future work will focus on automating mesh generation and L-curve evaluation to streamline integration into clinical and experimental workflows.

Funding

P. Livens acknowledges the support of the Research foundation Flanders (FWO) under grant nr. 1273723N. A. Bradu acknowledges the support of the Royal Society, project PARSOCT, RGS/R1/221324, and the support of the Academy of Medical Sciences/the Wellcome Trust/the Government Department of Business, Energy and Industrial Strategy/the British Heart Foundation/Diabetes UK Springboard Award SBF007\100162.

Disclosures

The authors declare no conflicts of interest.

Data availability statement

Matlab routines underlying the results presented in this paper are available in a dedicated repository: https://bitbucket.org/bimef/oct-filtering-using-global-fe/src/main/.

OCT and simulated data will be provided upon reasonable request.

Appendix

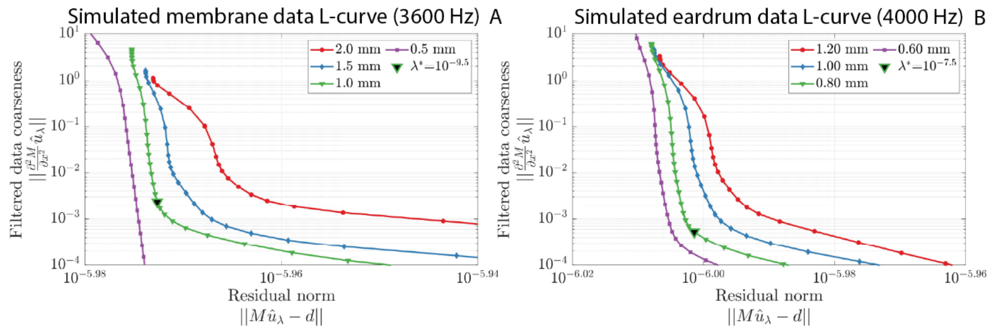

Fig. A1. L-curves for the membrane model at 3600 Hz (A), and for the eardrum model at 4000 Hz (B). For the membrane model, a Q9 mesh with element size of 1 mm leads to an L-shape, shown in green. For the eardrum data, a T6 mesh of 0.80 mm led to the clearest L-shape (B).

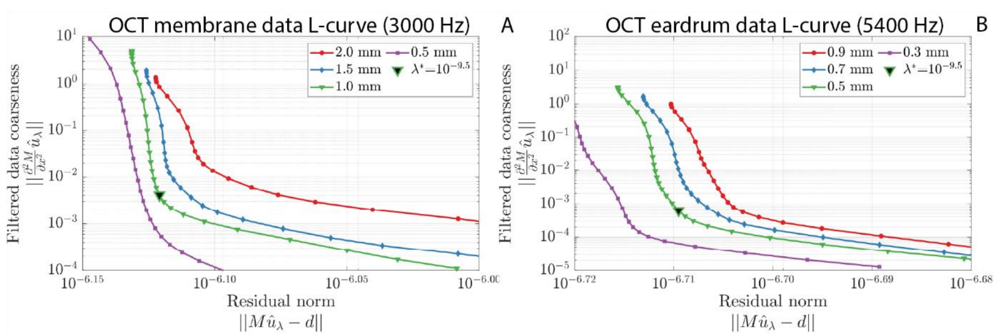

Fig. A2. L-curves for experimental data of the membrane at 3000 Hz (A), and for the eardrum data at 5400 Hz (B). For the membrane model (A), a Q9 mesh with element size of 1 mm was selected. For the eardrum data, a T6 mesh with edge-lengths of 0.5 mm was chosen, balancing spatial resolution with data filtering.

References

1. J. G. Fujimoto and W. Drexler, "Introduction to OCT," in *Optical Coherence Tomography*, W. Drexler and J. G. Fujimoto, eds. (Springer International Publishing, 2015), pp. 3–64.
2. M. Zeppieri, S. Marsili, E. S. Enaholo, A. O. Shuaibu, N. Uwagboe, C. Salati, L. Spadea, and M. Musa, "Optical Coherence Tomography (OCT): A Brief Look at the Uses and Technological Evolution of Ophthalmology," Medicina **59**(12), 2114 (2023).
3. M. A. Sadhin, A. K. Dadzie, M. Abtahi, B. Ebrahimi, A. H. Sadhin, T. Son, M. J. Heiferman, J. I. Lim, and X. Yao, "OCTA-ReVA^{+AV}: an open-source toolbox for retinal artery–vein segmentation and analysis in OCT angiography," Biomed. Opt. Express, BOE **16**(11), 4689–4700 (2025).
4. P. G. Daneshmand, H. Rabbani, and A. Mehridehnavi, "Super-Resolution of Optical Coherence Tomography Images by Scale Mixture Models," IEEE Trans. on Image Process. **29**, 5662–5676 (2020).
5. Z. Yuan, D. Yang, H. Pan, and Y. Liang, "Axial Super-Resolution Study for Optical Coherence Tomography Images Via Deep Learning," IEEE Access **8**, 204941–204950 (2020).
6. B. L. Frost, N. P. Janjušević, C. E. Strimbu, and C. P. Hendon, "Compressed sensing on displacement signals measured with optical coherence tomography," Biomed. Opt. Express, BOE **14**(11), 5539–5554 (2023).
7. J. Duan, W. Lu, C. Tench, I. Gottlob, F. Proudlock, N. N. Samani, and L. Bai, "Denoising optical coherence tomography using second order total generalized variation decomposition," Biomedical Signal Processing and Control **24**, 120–127 (2016).
8. A. Ramier, J. T. Cheng, M. E. Ravicz, J. J. Rosowski, and S.-H. Yun, "Mapping the phase and amplitude of ossicular chain motion using sound-synchronous optical coherence vibrography," Biomed. Opt. Express **9**(11), 5489 (2018).
9. E. W. Chang, J. B. Kobler, and S. H. Yun, "Subnanometer optical coherence tomographic vibrography," Opt. Lett. **37**(17), 3678 (2012).
10. W. Dong and S. W. F. Meenderink, "Imaging the Ear Anatomy and Function Using Optical Coherence Tomography Vibrometry," Semin Hear **45**(01), 101–109 (2024).
11. W. Kim, S. Kim, S. Huang, J. S. Oghalai, and B. E. Applegate, "Picometer scale vibrometry in the human middle ear using a surgical microscope based optical coherence tomography and vibrometry system," Biomed. Opt. Express, BOE **10**(9), 4395–4410 (2019).
12. W. Kim, D. Liu, S. Kim, K. Ratnayake, F. Macias-Escriva, S. Mattison, J. S. Oghalai, and B. E. Applegate, "Vector of motion measurements in the living cochlea using a 3D OCT vibrometry system," Biomed. Opt. Express **13**(4), 2542 (2022).
13. E. S. Olson and C. E. Strimbu, "Cochlear mechanics: new insights from vibrometry and optical coherence tomography," Current Opinion in Physiology **18**, 56–62 (2020).
14. S. Van der Jeught, J. J. J. Dirckx, J. R. M. Aerts, A. Bradu, A. G. Podoleanu, and J. A. N. Buytaert, "Full-Field Thickness Distribution of Human Tympanic Membrane Obtained with Optical Coherence Tomography," JARO **14**(4), 483–494 (2013).
15. M. Koch, T. M. Eßinger, H. Maier, J. H. Sim, L. Ren, N. T. Greene, T. Zahnert, M. Neudert, and M. Bornitz, "Methods and reference data for middle ear transfer functions," Sci Rep **12**(1), 17241 (2022).
16. A. Burkhardt, L. Kirsten, M. Bornitz, T. Zahnert, and E. Koch, "Investigation of the human tympanic membrane oscillation ex vivo by Doppler optical coherence tomography," Journal of Biophotonics **7**(6), 434–441 (2014).

17. S. Avril, P. Feissel, F. Pierron, and P. Villon, "Comparison of two approaches for differentiating full-field data in solid mechanics," Meas. Sci. Technol. **21**(1), 015703 (2010).
18. F. S. M. Pires, S. Avril, P. Livens, J. A. Cordioli, and J. J. J. Dirckx, "Material Identification on Thin Shells Using the Virtual Fields Method, Demonstrated on the Human Eardrum," J Biomech Eng. **144(3)**, (2021).
19. T. Fourest, "Optimizing Metrological Efficiency: Comparative Analysis of Filtering Methods for 2D DIC," Exp Tech **48**(5), 921–934 (2024).
20. F. Hild and S. Roux, "Comparison of Local and Global Approaches to Digital Image Correlation," Exp Mech **52**(9), 1503–1519 (2012).
21. T. Fourest, "Optimizing Metrological Efficiency: Comparative Analysis of Filtering Methods for 2D DIC," Exp Tech **48**(5), 921–934 (2024).
22. A. Peshave, F. Pierron, P. Lava, D. Moens, and D. Vandepitte, "Practical Uncertainty Quantification Guidelines for DIC-Based Numerical Model Validation," Exp Tech **49**(3), 437–457 (2025).
23. P. Livens and E. Ukshini, "Comparing Local Versus Global Filtering Techniques on Fast Pressure-Sensitive Paint Data," Exp Tech (2025).
24. J. Cornelis and W. Vanroose, "Projected Newton method for noise constrained ℓ_p regularization," Inverse Problems **36**(12), 125004 (2020).
25. R. Yang, "A regularized finite-element digital image correlation for irregular displacement field," Optics and Lasers in Engineering **56**, 67–73 (2014).
26. C. Cofaru, W. Philips, and W. Van Paepegem, "A novel speckle pattern—Adaptive digital image correlation approach with robust strain calculation," Optics and Lasers in Engineering **50**(2), 187–198 (2012).
27. C. De Boor, *A Practical Guide to Splines*, Applied Mathematical Sciences (Springer, 2001).
28. P. G. G. Muyshondt and J. J. J. Dirckx, "How does prestrain in the tympanic membrane affect middle-ear function? A finite-element model study in rabbit," Journal of the Mechanical Behavior of Biomedical Materials **131**, 105261 (2022).
29. P. G. G. Muyshondt and J. J. J. Dirckx, "Structural stiffening in the human middle ear due to static pressure: Finite-element analysis of combined static and dynamic middle-ear behavior," Hearing Research **400**, 108116 (2021).
30. P. Livens, P. G. G. Muyshondt, and J. J. J. Dirckx, "Prestrain in the rabbit eardrum measured by digital image correlation and micro-incisions," Hearing Research **412**, 108392 (2021).
31. P. Livens and J. J. J. Dirckx, "Rabbit tympanic membrane thickness distribution obtained via optical coherence tomography," Hearing Research **429**, 108701 (2023).
32. P. Livens and J. J. J. Dirckx, "Prestrain in the eardrum investigated using laser-ablation perforation: A proof of principle study on the New Zealand white rabbit," Hearing Research **437**, 108840 (2023).
33. H. C. Hendargo, R. P. McNabb, A.-H. Dhalla, N. Shepherd, and J. A. Izatt, "Doppler velocity detection limitations in spectrometer-based versus swept-source optical coherence tomography," Biomed. Opt. Express **2**(8), 2175 (2011).
34. R. K. Wang and A. L. Nuttall, "Phase-sensitive optical coherence tomography imaging of the tissue motion within the organ of Corti at a subnanometer scale: a preliminary study," J Biomed Opt **15**(5), 056005 (2010).
35. W. Drexler and J. G. Fujimoto, eds., *Optical Coherence Tomography: Technology and Applications* (Springer International Publishing, 2015).

36. A. Bradu, N. M. Israelsen, M. Maria, M. J. Marques, S. Rivet, T. Feuchter, O. Bang, and A. Podoleanu, "Recovering distance information in spectral domain interferometry," Sci Rep **8**(1), (2018).
37. G. Nteroli, A. Podoleanu, and A. Bradu, "Master-slave enhanced optical coherence microscopy for real-time optical biopsy imaging," in *Clinical Biophotonics III*, D. S. Elson, S. Gioux, and B. W. Pogue, eds. (SPIE, 2024), p. 30.
38. L. Abbott, G. Nteroli, R. D. Engelsholm, P. B. Montague, A. Podoleanu, and A. Bradu, "Balanced-detection visible optical coherence tomography with a low-noise supercontinuum laser," Biomed. Opt. Express **16**(7), 2898 (2025).
39. D. Chapelle and K.-J. Bathe, *The Finite Element Analysis of Shells — Fundamentals*, Computational Fluid and Solid Mechanics (Springer Berlin Heidelberg, 2003).
40. N. K. Ojha, R. K. Saxena, G. Vashishtha, and S. Chauhan, "Fracture Prediction in Weldox 700E Steel Subjected to High Velocity Impact Using LS-DYNA," Applied Sciences **15**(7), 3677 (2025).
41. P. Liu, S. Steuer, J. Golde, J. Morgenstern, Y. Hu, C. Schieffer, S. Ossmann, L. Kirsten, S. Bodenstedt, M. Pfeiffer, S. Speidel, E. Koch, and M. Neudert, "The Dresden in vivo OCT dataset for automatic middle ear segmentation," Sci Data **11**(1), 242 (2024).
42. J. Tian, B. Varga, G. M. Somfai, W.-H. Lee, W. E. Smiddy, and D. Cabrera DeBuc, "Real-Time Automatic Segmentation of Optical Coherence Tomography Volume Data of the Macular Region," PLoS ONE **10**(8), e0133908 (2015).
43. R. Straughan, K. Kadry, S. A. .Parikh, E. R. Edelman, and F. R. Nezami, "Fully automated construction of three-dimensional finite element simulations from Optical Coherence Tomography," Computers in Biology and Medicine **165**, 107341 (2023).
44. S. Kindermann and K. Raik, "A simplified L-curve method as error estimator," etna **53**, 217–238 (2020).